

Boise State University

ScholarWorks

Geosciences Faculty Publications and
Presentations

Department of Geosciences

12-2023

Geophysics-Informed Hydrologic Modeling of a Mountain Headwater Catchment for Studying Hydrological Partitioning in the Critical Zone

Hang Chen

Boise State University

Qifei Niu

Boise State University

Aida Mendieta

Sorbonne Université

John Bradford

Colorado School of Mines

James McNamara

Boise State University

Water Resources Research®



RESEARCH ARTICLE

10.1029/2023WR035280

Key Points:

- The 3D velocity model of a mountain catchment was created based on the results of a series of 2D seismic refraction tests
- The 3D subsurface critical zone structure was extracted from the velocity model and incorporated into hydrologic modeling
- Geophysics-informed hydrologic modeling provides valuable additional information on the hydrological partitioning in the catchment

Supporting Information:

Supporting Information may be found in the online version of this article.

Correspondence to:

Q. Niu,
qifeiniu@boisestate.edu

Citation:

Chen, H., Niu, Q., Mendieta, A., Bradford, J., & McNamara, J. (2023). Geophysics-informed hydrologic modeling of a mountain headwater catchment for studying hydrological partitioning in the critical zone. *Water Resources Research*, 59, e2023WR035280. <https://doi.org/10.1029/2023WR035280>




Received 5 MAY 2023

Accepted 9 NOV 2023

Author Contributions:

Conceptualization: Qifei Niu
Data curation: Aida Mendieta, John Bradford, James McNamara
Formal analysis: Hang Chen
Funding acquisition: Qifei Niu
Investigation: Hang Chen, Aida Mendieta, John Bradford, James McNamara
Methodology: Hang Chen, Qifei Niu, James McNamara
Project Administration: Qifei Niu

Geophysics-Informed Hydrologic Modeling of a Mountain Headwater Catchment for Studying Hydrological Partitioning in the Critical Zone

Hang Chen¹ , Qifei Niu¹ , Aida Mendieta², John Bradford³, and James McNamara¹ 

¹Department of Geosciences, Boise State University, Boise, ID, USA, ²CNRS, EPHE, UMR 7619 METIS, Sorbonne Université, Paris, France, ³Department of Geophysics, Colorado School of Mines, Golden, CO, USA

Abstract Hydrologic modeling has been a useful approach for analyzing water partitioning in catchment systems. It will play an essential role in studying the responses of watersheds under projected climate changes. Numerous studies have shown it is critical to include subsurface heterogeneity in the hydrologic modeling to correctly simulate various water fluxes and processes in the hydrologic system. In this study, we test the idea of incorporating geophysics-obtained subsurface critical zone (CZ) structures in the hydrologic modeling of a mountainous headwater catchment. The CZ structure is extracted from a three-dimensional seismic velocity model developed from a series of two-dimensional velocity sections inverted from seismic travel time measurements. Comparing different subsurface models shows that geophysics-informed hydrologic modeling better fits the field observations, including streamflow discharge and soil moisture measurements. The results also show that this new hydrologic modeling approach could quantify many key hydrologic fluxes in the catchment, including streamflow, deep infiltration, and subsurface water storage. Estimations of these fluxes from numerical simulations generally have low uncertainties and are consistent with estimations from other methods. In particular, it is straightforward to calculate many hydraulic fluxes or states that may not be measured directly in the field or separated from field observations. Examples include quickflow/subsurface lateral flow, soil/rock moisture, and deep infiltration. Thus, this study provides a useful approach for studying the hydraulic fluxes and processes in the deep subsurface (e.g., weathered bedrock), which needs to be better represented in many earth system models.

Plain Language Summary The precipitation received in a watershed is usually partitioned into streamflow, plant water use, soil/rock moisture, and groundwater. While many of these components can be directly measured in the field or estimated from hydrometeorological measurements, the moisture stored in the subsurface (soil and rock layers) is difficult to quantify and measure. Using the computer to simulate the water flow and storage in a watershed provides a useful tool for quantifying water partitioning in a catchment. Previous research highlighted the importance of including both above-ground and below-ground variations in computational modeling. Compared to above-ground heterogeneity, it is much more challenging to characterize below-ground heterogeneity because we cannot see the variations in the subsurface. In this study, we propose to determine the subsurface heterogeneity/variability with geophysical imaging (more specifically, the seismic refraction method), and the geophysics-obtained subsurface model is then incorporated into the computational simulation of a watershed or catchment. A small mountainous headwater catchment in Idaho is used to demonstrate this method, and the results show that the new modeling well reproduces the field-measured streamflow of the catchment. This new modeling also gives reliable estimates for some properties that are difficult to determine using traditional methods. With the changing climate, the proposed new method will help better understand how a catchment will respond to the projected weather, such as extreme snowfalls or severe droughts.

1. Introduction

In the western United States, urban and agricultural water uses largely depend on the surface water and groundwater that are generated and recharged from mountainous catchments (Bales et al., 2006). With increases in water usage and climate change, making more informed decisions to manage water resources in these regions is imperative. In particular, most of the stream water in the western United States is supplied by seasonal snow, which is at risk from a warming climate (Barnett et al., 2005). In these catchments, precipitation is partitioned into various

© 2023. The Authors.

This is an open access article under the terms of the [Creative Commons Attribution-NonCommercial-NoDerivs License](https://creativecommons.org/licenses/by/4.0/), which permits use and distribution in any medium, provided the original work is properly cited, the use is non-commercial and no modifications or adaptations are made.

Resources: Qifei Niu
Software: Hang Chen
Supervision: Qifei Niu
Validation: Hang Chen
Visualization: Hang Chen
Writing – original draft: Hang Chen
Writing – review & editing: Qifei Niu, Aida Mendieta, James McNamara

processes, including evapotranspiration (ET), streamflow, deep infiltration, and subsurface storage (Aishlin & McNamara, 2011; Rempe & Dietrich, 2018). As pointed out in P. D. Brooks et al. (2015), there is still a common knowledge gap in how precipitation is partitioned in the critical zone (CZ), which encompasses the vertical domain from the base of active groundwater circulation through the top of vegetation canopies and horizontal domains with nested catchments associated with surface and subsurface structure (P. D. Brooks et al., 2015). Therefore, understanding and predicting hydrological partitioning in mountainous catchments is critically needed so that best management practices can be implemented to adapt to climate change.

Hydrologic modeling is commonly used to study the partitioning of water in mountainous catchments (e.g., Paniconi & Putti, 2015). The accuracy of hydrologic modeling for predicting hydrologic responses of a catchment largely depends on process representation and parameterization (Camporese et al., 2019). While the representation of individual hydrologic processes has advanced significantly over the years (Clark et al., 2015), improved representations of heterogeneity in hydrologic modeling are still critically needed, especially the subsurface structural heterogeneity. In mountainous terrains, the subsurface CZ structure (i.e., the depth extent of various CZ layers) is one of the most significant sources of subsurface structural heterogeneity. Many hydrologic models only consider water movement in the shallow soil layer in simulating the streamflow generation and water storage in headwater catchments (e.g., Muhammad et al., 2019). However, recent studies have highlighted the role of the fractured/weathered bedrock layer and its complex geometry on subsurface water storage (Rempe & Dietrich, 2018) and streamflow generation (Camporese et al., 2019; Masaoka et al., 2021). Therefore, incorporating accurate subsurface structure is crucial for hydrologic modeling of water partitioning in mountainous catchments.

In the Earth's CZ, weathering transforms fresh bedrock into the regolith. Due to complex influences from tectonic stress, lithology, and climatic forcing, the subsurface of the CZ exhibits heterogeneous features (Riebe et al., 2017). In general, the subsurface of the CZ consists of three distinct layers, regolith, fractured or weathered bedrock, and fresh bedrock (e.g., St. Clair et al., 2015). While the regolith has a typical thickness of several meters (Callahan et al., 2020; Hayes et al., 2019; Nielson, Bradford, Holbrook, & Seyfried, 2021; Nielson, Bradford, Pierce, & Seyfried, 2021), the fractured bedrock can span over tens of meters. In addition, the thickness of each layer varies considerably in the horizontal direction (e.g., Patton et al., 2018), and process-based models to give accurate predictions of the CZ structures are not yet available.

Direct methods such as borehole drilling and soil pit sampling have often been used to characterize the CZ structure (e.g., Hahm et al., 2019; Rempe & Dietrich, 2018). However, these methods are costly and labor-intensive, and thus it is impractical to use them for determining the fine-scale CZ structures for hydrologic modeling. Recently, geophysical imaging has been successfully used in CZ science due to its noninvasive nature and low cost (Parsekian et al., 2015), and they have the potential to accelerate CZ studies by providing subsurface information at vertical scales ranging from centimeters to hundreds of meters and at lateral scales from meters to kilometers (Parsekian et al., 2015). Various geophysical imaging methods can be used for different purposes in CZ studies. For instance, in CZ hydrology, electrical resistivity tomography has been commonly used to estimate the moisture content (Nielson, Bradford, Holbrook, & Seyfried, 2021; Nielson, Bradford, Pierce, & Seyfried, 2021) and monitor subsurface water dynamics (Guo et al., 2020); this is because the electrical resistivity of geological materials is strongly influenced by the amount of water stored in the pore space. Another example is seismic refraction imaging, which can give spatial distributions of the seismic velocity of the subsurface. Since different CZ layers (regolith, fractured rock, and fresh bedrock) have distinct velocities (Flinchum et al., 2022), the seismic refraction method has become a standard way to gain subsurface structural information in CZ studies (e.g., Flinchum et al., 2018; St. Clair et al., 2015).

In this study, we incorporate CZ structures extracted from geophysical imaging into hydrologic modeling of mountain headwater catchments to evaluate if the geophysics-informed hydrologic modeling provides improved information on water partitioning in the CZ. In particular, we analyze how the subsurface storage is partitioned into soil moisture and rock moisture and how individual components vary seasonally. In this paper, we first introduce the site condition and relevant hydrometeorological data sets as well as provide a short review of water partitioning studies at the study site. We then describe the seismic refraction tests performed at the site and the detailed data processing procedures for constructing the three-dimensional (3D) velocity model. The approach for extracting CZ structure information from the velocity model is then presented, followed by the calibration and validation of the hydrologic modeling. We evaluate the performance of this geophysics-informed hydrologic modeling by

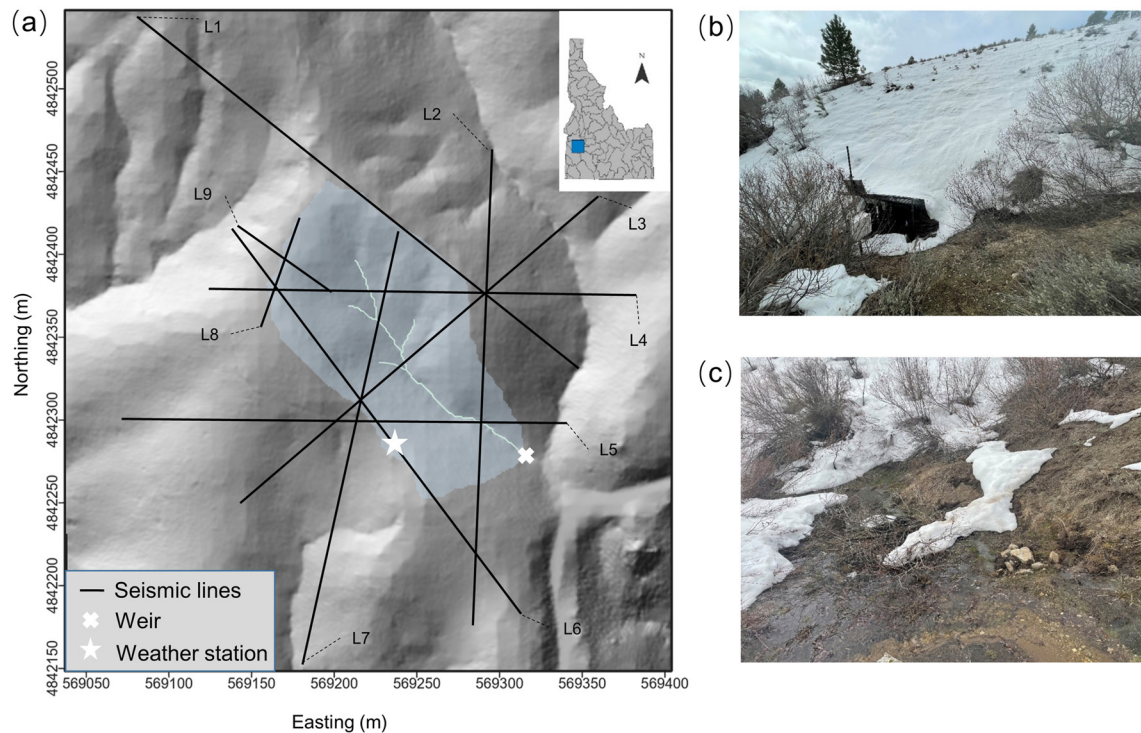


Figure 1. The headwater catchment (Treeline site) used in this study: (a) a hillshaded image of the catchment (highlighted in light blue) and nearby regions, including the locations of the seismic refraction tests, and (b) a picture showing the snow accumulation in a typical winter, and (c) a picture showing the snowmelt-induced streamflow. Hydrometeorological data used in this study were from the weather station and weir, shown in panel (a).

comparing its simulation results to other hydrologic modeling results that incorporate no or limited subsurface information. The hydrological partitioning in the CZ determined from the simulation is also discussed. Major conclusions are summarized at the end of the paper.

2. Study Site and Field Data

2.1. Site Condition

This study used a headwater catchment (Treeline site) in the Dry Creek Experimental Watershed (DCEW). The DCEW, ~ 27 km², is located at the southwestern margin of the Atlanta lobe of the Idaho batholith in Idaho, US (Clayton et al., 1979; McNamara et al., 2018). The elevation of the watershed ranges from 1,030 m to 2,130 m, and it encompasses both snow-dominated higher-elevation forests and rain-dominated lower-elevation grasslands. The Treeline catchment (Figure 1) is located at the snow-to-rain transition zone and has an average elevation of 1,620 m (Kormos et al., 2014). The drainage area of the catchment is ~ 0.02 km² and the intermittent stream (Figure 1) flows mainly during the snow seasons. The northeast slope of the catchment ranges from 26° to 39°, and the southwest slope ranges from 17° to 31°.

Precipitation in the catchment mainly occurs during the spring, autumn, and winter, while the summer is generally dry (McNamara et al., 2018). Nearly half of the winter precipitation is in the form of snow or a mixed event (McNamara et al., 2018), and snowmelt water is one of the major sources of streamflow (Figure 1c). The vegetation in the catchment includes Wyoming Big Sagebrush (*Artemisia tridentata*), Buckbrush (*Ceanothus velutinus*), Chokecherry (*Prunus virginiana*), and various forbs, shrubs, and grasses (Kormos et al., 2014). The annual precipitation and discharge of the catchment are 641 and 96 mm (McNamara et al., 2011), respectively.

The bedrock of the catchment is granodiorite of Cretaceous-Paleogene age (Clayton et al., 1979), and the soil is mainly formed by in-situ weathering of the underlying granitic bedrock. The soils are classified primarily as sand and sandy loam (Gribb et al., 2009). Previous field sampling surveys showed that the soil layer is relatively thin, ranging from tens of centimeters to ~ 2 m (Poulos, 2016). Fractures are widespread in the bedrock according

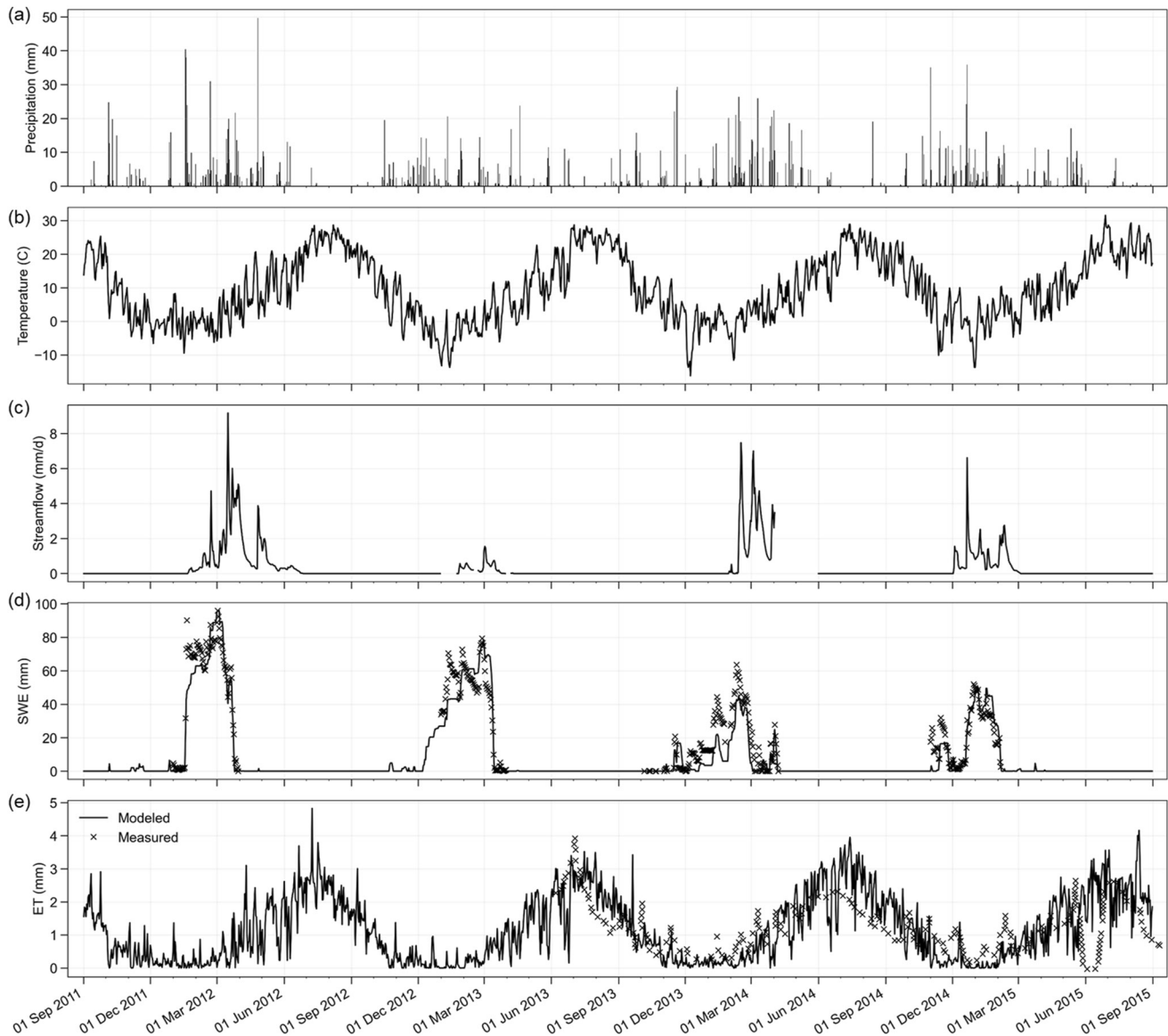


Figure 2. Daily hydrometeorological data at the catchment from 2011 to 2015: (a) precipitation, (b) temperature, (c) streamflow, (d) snow water equivalence (SWE), and (e) potential evapotranspiration. In (d), data points indicate field-measured SWE, and the solid line is the simulation from the Snow-17 model (Anderson, 2006) calibrated with field SWE data. In (e), data points are MODIS evapotranspiration (ET) measurements, and the solid line is the potential ET calculated using the Penman-Monteith equation.

to previous geophysical studies (e.g., Miller et al., 2008), but it is unclear how the fractured bedrock is spatially distributed.

2.2. Hydrometeorological Data

The hydrometeorological conditions of the catchment have been instrumented since 1998 with a weather station and a weir shown in Figure 1a. Data of the water years from 2012 to 2015 (Figure 2) are used for our study. These four years consist of a range of weather conditions, including the relatively wetter 2011–2012 winter and the drier 2014–2015 winter. The datasets include daily precipitation (Figure 2a), temperature (Figure 2b), streamflow (Figure 2c), and snow water equivalence (SWE) (Figure 2d). In Figure 2d, an increased SWE is calculated as the product of new fallen snow depth h_{ns} and snow density ρ_{ns} ; the measured snow density $\rho_{ns} = 0.16 \text{ g/cm}^3$ (Boe, 2013) is used for newly fallen snow, and the density of old snow is assumed not changing with time.

The reference ET (ET_0) in the catchment was estimated with the Penman-Monteith equation (Allen et al., 1998) using field-monitored meteorological data. The reference ET_0 in the Penman-Monteith equation is expressed as

$$ET_0 = \frac{0.408\Delta(R_n - G) + \gamma \frac{900}{T+273} u_2 (e_s - e_a)}{\Delta + \gamma(1 + 0.34u_2)}, \quad (1)$$

where R_n is the net radiation at the crop surface, G is the soil heat flux density, T is the mean daily air temperature 2 m above the ground, u_2 is the wind speed 2 m above the ground, e_s is the saturation vapor pressure, e_a is the actual vapor pressure, Δ is the slope of the vapor pressure curve, and γ is psychrometric constant. The reference ET (ET_0) can be linked to potential ET (ET_p) by a crop coefficient K_c , expressed as

$$ET_p = K_c ET_0. \quad (2)$$

During wet seasons (e.g., from March to May), the actual ET (ET_a) is assumed to be equal to potential ET (ET_p), and we use ET_a measured from MODIS at a nearby site (Kraft & McNamara, 2022; see data points in Figure 2e) to determine the crop factor K_c by fitting the calculated ET_p during the wet season to ET_a . The calculated daily potential ET (ET_p) at the catchment is plotted in Figure 2e.

2.3. Insights From Previous Investigations at the Study Site

This study builds on a history of investigations at the Treeline site, where assumptions and knowledge about how subsurface structure impacts streamflow have gradually improved. McNamara et al. (2005) suggested that ephemeral streamflow initiates when infiltrating rain or snowmelt reaches impermeable bedrock beneath the deepest hillslope soils, and hillslopes become hydraulically connected to the stream. The fallacy of the impermeable bedrock assumption became clear when Aishlin and McNamara (2011) used a chloride mass balance to show that approximately 35% of annual precipitation does not exit the catchment as evapotranspiration or streamflow but as leakage into the underlying bedrock. Kelleners et al. (2009) developed a one-dimensional physically-based model of the plant-soil continuum and independently confirmed that approximately 40% of annual precipitation was unaccounted for in the soil column. In a subsequent two-dimensional model (Kelleners et al., 2010), successful streamflow simulations were achieved only when bedrock conductivity was representative of highly fractured granite. Kelleners et al.'s (2010) work estimated that 34%–36% of the incoming precipitation leaves the catchment as bedrock infiltration, and only 11%–16% is transformed into streamflow. Kormos et al. (2014, 2015) used a physically-based snowmelt model to develop distributed estimates of water delivery to the soil surface across the catchment and then delivered simulated water inputs to a conceptual soil moisture storage model using soil depth measurements from Williams et al. (2009). Catchment-scale bedrock infiltration was estimated by subtracting annual streamflow from the sum of distributed deep drainage from the soil. They showed again that approximately 34% of annual precipitation is partitioned to deep drainage. These studies indicate that the bedrock at the Treeline site is hydrologically active but poorly constrained.

Some geophysical works have been carried out in or near the DCEW to characterize the subsurface structure and water storage dynamics. For instance, Miller et al. (2008) conducted time-lapse electrical resistivity surveys at the Treeline catchment, and they identified a bedrock infiltration pathway that had previously been inferred from hydrological studies but was not well understood. Mendieta (2017) performed a series of seismic refraction tests at the Treeline catchment and nearby sites and found that the depth of fractured bedrock can reach up to tens of meters; the seismic velocity results also imply that the hydrologic properties of the fractured bedrock at the site may be anisotropic. These geophysical studies indicated that the fractured bedrock at DCEW plays a significant role in affecting the subsurface water transmission and storage.

3. Extracting CZ Structures From Seismic Results

In this section, we first introduce the seismic refraction tests and the relevant inversion results, followed by a 3D seismic velocity model for the catchment. We then explain the procedures used to extract subsurface structures from the 3D velocity model. The geophysics-determined soil (or regolith) depth is also compared to field-measured soil depth from previous soil surveys.

3.1. Seismic Refraction Tests and Inversion

A series of seismic refraction tests have been carried out in the catchment to characterize the CZ structures, and the locations of these survey lines are shown in Figure 1a. All the seismic refraction data were acquired using the Geode system (Geometrics Inc., CA, USA) with a sledgehammer as the seismic source. Survey lines from L1 to L7 were collected from the fall of 2015 to the fall of 2016 with 72 geophones (5 m spacing), and seismic sources were spaced 20 m apart (Mendieta, 2017). Survey lines L8 and L9 were carried out in June 2020 with 72 geophones (1 m spacing), and the seismic source spacing varied between 12 and 30 m (Chen & Niu, 2022).

The first arrival time was manually picked for all the traces measured by the geophones. The travel time data of each survey line are inverted using the pyGIMLi software package (Rücker et al., 2017) to reconstruct the 2D velocity model. In forward modeling, the finite element method calculates travel times based on a given velocity model, and the shortest path algorithm is used for ray tracing through the meshes (Dijkstra, 1959; Moser, 1991). The smoothness regularization was imposed to stabilize or constrain the inversion. In the CZ, the structural variation in the vertical direction is usually much larger than that in the horizontal direction; to account for this, an anisotropic smoothness regularization was imposed (Jiang et al., 2020; Wagner & Uhlemann, 2021). In the inversion, the velocity model was updated iteratively using the Gauss-Newton method until the data misfit reached a predefined value. In this study, the average root mean square deviation (RMSD) of observed and simulated travel times is generally less than 3 ms for all the seismic lines.

The inverted 2D velocity models are plotted in the shaded relief map (Figure 3a) to better visualize spatial velocity distribution in the catchment. A typical 2D velocity model is shown in Figure 3b, and Figure S1 in Supporting Information S1 summarizes all the individual 2D velocity models. In Figure 3c, we plotted a velocity profile along the elevation to demonstrate how the velocity varies with the elevation in the CZ. As shown in Figure 3c, we used $v_p = 1.2 \text{ km s}^{-1}$ and 3.5 km s^{-1} to represent the regolith-fractured bedrock and fractured-intact bedrock interfaces (see Section 3.3 for the determination of these two velocity values). The selection of these two velocity values is consistent with some previous work on granitic bedrock. For instance, Flinchum et al. (2018) used $v_p = 1.2 \text{ km s}^{-1}$ and 4 km s^{-1} to represent the regolith bottom and weathered bedrock bottom, respectively, at a granitic site.

Using these two representative velocity contours, we can infer the heterogeneous subsurface CZ structures (i.e., the depth extent of regolith and weathered bedrock) from the 2D velocity models in Figure 3a. In general, most of the 2D velocity models show similar features: the base of regolith (including soil and saprolite) is roughly in parallel with the ground surface; in contrast, the base of the weathered bedrock mirrors the ground surface. This type of subsurface CZ structure has been found in other studies (e.g., St. Clair et al., 2015), and it was attributed to the stress condition of the subsurface (Moon et al., 2017; St. Clair et al., 2015). According to the theory proposed by St. Clair et al. (2015), the stress in the bedrock allows abundant fractures to grow or open, providing pathways for water and biota to invade the bedrock and initiate weathering (Riebe et al., 2017). Considering the topographic perturbations, this theory predicts that the base of the fractured bedrock mirrors the surface topography when the ratio of horizontal compressive stresses over the vertical gravitational stress is relatively large, and it parallels the surface topography when the ratio is relatively small. Therefore, the 2D velocity-inferred subsurface CZ structure at the site implies that the horizontal stress at the site is relatively larger than the vertical gravitational stress. Since the regional tectonic stress is generally under tension (Bennett, 1986), this implies that the stress field at the site may be distorted by some local stress anomalies (e.g., from geological structure; Reynolds et al., 2005).

3.2. 3D Seismic Velocity Model

These nine 2D velocity models (Figure 3a) are used to estimate the 3D velocity distribution in the subsurface of the catchment with the ordinary Kriging (e.g., Bourges et al., 2012). We used the GSTools toolbox (Müller et al., 2021) and followed the procedures proposed by Flinchum et al. (2018) to construct the 3D velocity model. One advantage of using GSTools is that the topography can be kept during the Kriging such that estimated velocities near the ground surface have low uncertainties. In Kriging, we first conducted variogram analysis to determine the spatial correlations of the subsurface velocity based on 2D velocity models. For each model, subsurface velocity values were sampled at every 3 m along the survey line and every 1 m along the depth. Velocity at locations with low sensitivity was excluded from our analysis. This resulted in a total number of 31,404 velocity

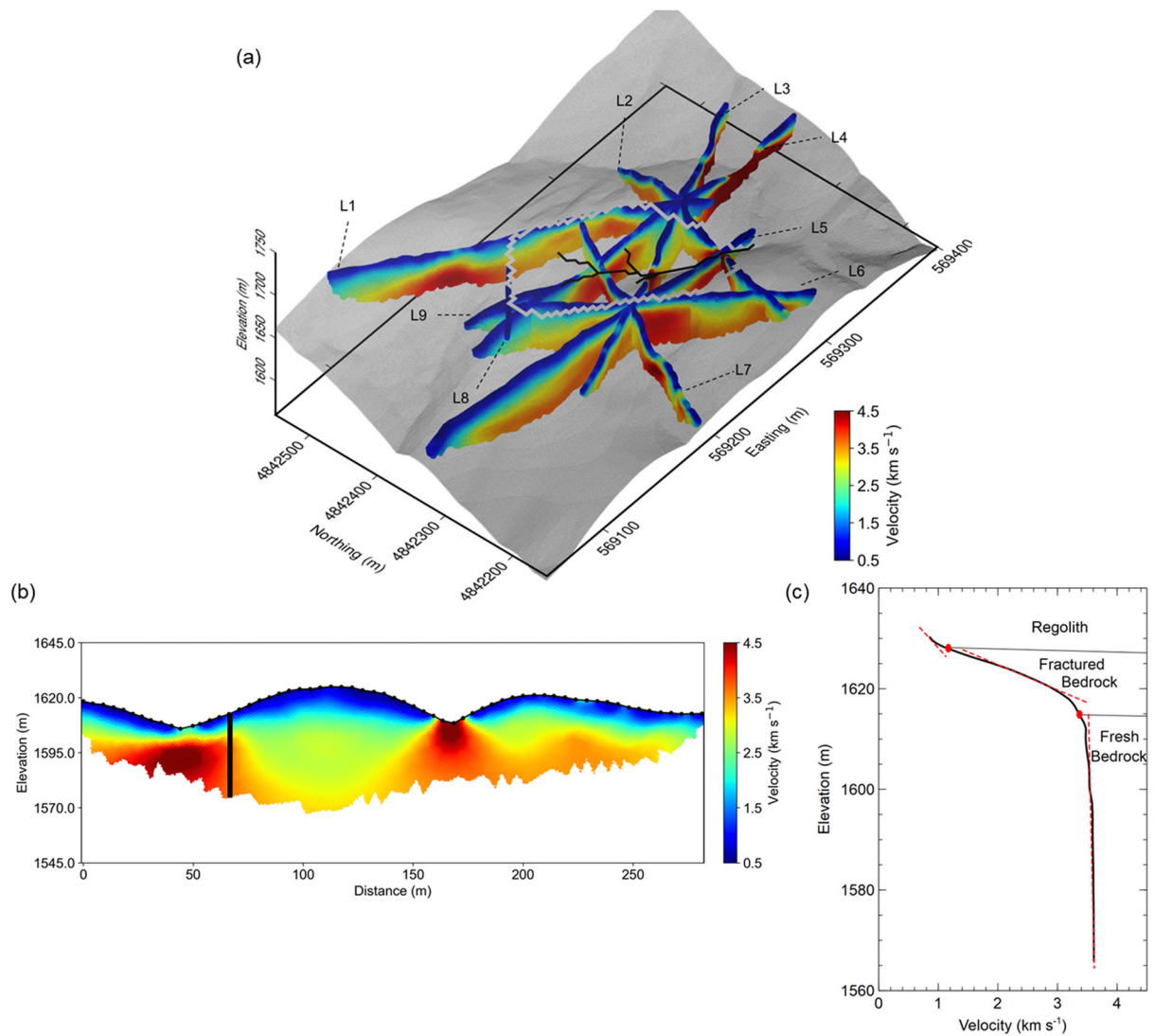


Figure 3. Inversion results of the 2D seismic refraction tests: (a) nine 2D velocity sections plotted in the shaded relief map of the catchment and nearby regions, (b) a typical 2D velocity model (L3), and (c) a typical velocity-elevation profile from (b) at the horizontal location marked by the solid line. In (c), dash red lines represent constant velocity gradients, which are used to determine the regolith-fractured bedrock interface and the bottom of fractured bedrock. The boundary of the catchment (white line) and the location of streams (black line) are also shown in panel (a).

data points. While 80% of these data points were used to calculate the experimental variograms, the rest 20% were used to verify the Kriging results.

We calculated 57 experimental variograms at 19 azimuths ranging from 0° to 180° and at three dips (0°, 5°, and 10°). The experimental variograms were fitted with the exponential covariance model (Webster & Oliver, 2007)

$$v(h) = C_0 + C_1[1 - \exp(-h/A)], \quad (3)$$

where v is the variogram, h is the lag distance, C_0 is the nugget, C_1 is the sill, and A is the range. In GSTools, C_1 is described by the square of variance; A is described by length scales and angles; and the nugget is generally considered as 0 (Flinchum et al., 2018). The length scales include three directions (i.e., L_x , L_y , and L_z), and the angles are known as Tait–Bryan angles given by yaw, pitch, and roll (Diebel, 2006). The Monte Carlo simulation is used to sample the parameters of the exponential covariance model (Equation 3), and the ranges of these parameters are listed in Table S1 of Supporting Information S1. We did 100,000 runs of samplings and selected 20 models with the lowest RMSD between the modeled and experimental variograms. The modeled variograms were then verified using the remaining 20% of the velocity data points. The comparison shows that the related

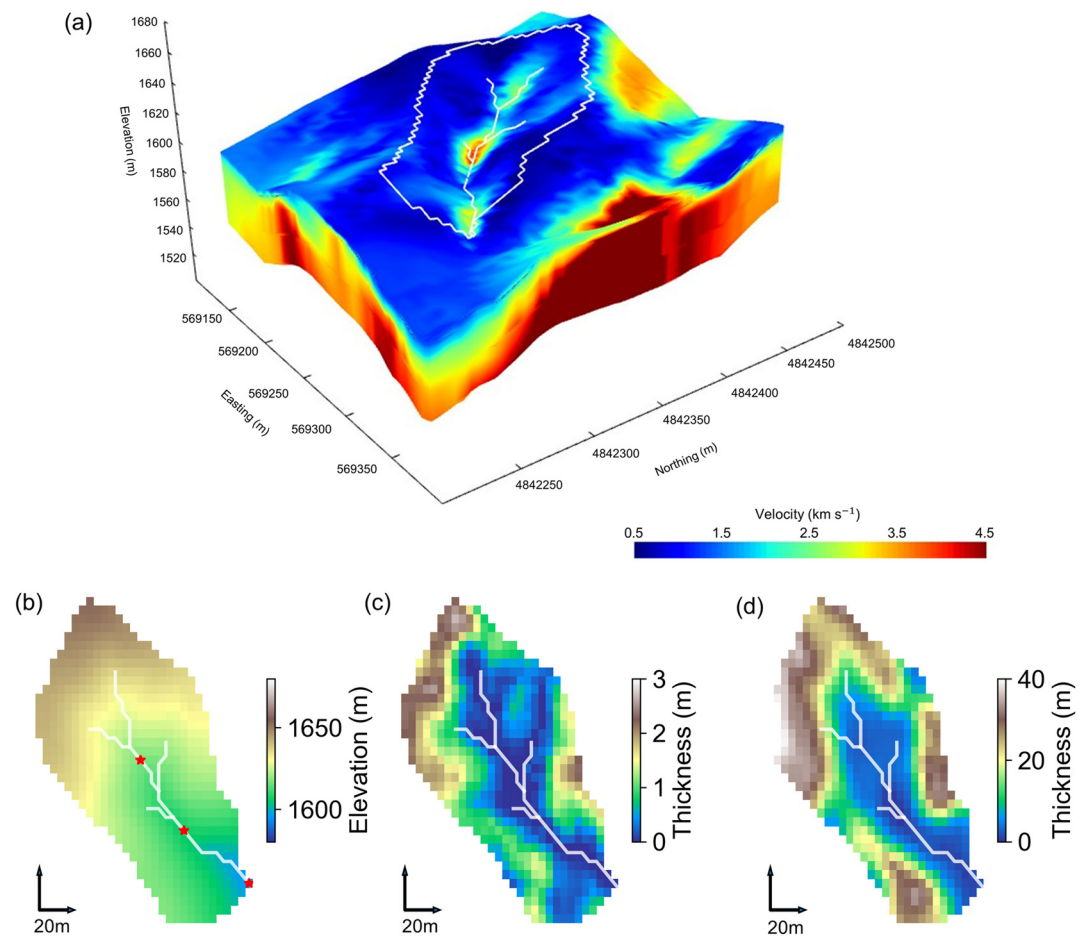


Figure 4. The reconstructed 3D seismic velocity model for the catchment (including surrounding area) and the extracted critical zone (CZ) structures: (a) 3D velocity distribution obtained from Kriging, (b) elevation map of the catchment, (c) regolith thickness distribution in the catchment, and (d) fractured bedrock thickness distribution in the catchment. The origins in (b), (c), and (d) are at Easting 569,243 m and Northing 4,842,061 m. The red crosses in panel (b) indicate three locations where the simulated groundwater level is reported (Figure 8b). The catchment boundary and locations of the stream are also included in the figures.

RMSDs are small, generally $<0.2 \text{ km s}^{-1}$. Among these 20 models, we selected a model with an RMSD of 0.18 km s^{-1} , and the relevant model parameters are also listed in Table S1 of Supporting Information S1.

The constructed 3D velocity model for the catchment is shown in Figure 4a, in which velocity artifacts (i.e., the velocity with high uncertainty) were removed (Flinchum et al., 2018). The uncertainty is evaluated with the Kriging variance, which measures the distance difference between measured data and calculated data from the model. The variance ranges from 0 to $0.74 \text{ km}^2 \text{ s}^{-2}$, and we removed velocities with Kriging variance greater than $0.4 \text{ km}^2 \text{ s}^{-2}$. The removed velocities were interpolated with velocity values at nearby locations.

3.3. CZ Structure Model and Validation

The current practice of extracting CZ structures from the velocity model is to select representative contour lines for CZ structural boundaries (e.g., regolith-fractured bedrock interface or fractured-intact bedrock interface) (e.g., Flinchum et al., 2018). Regarding how to pick these representative velocity values, there are, however, no standard ways. Sometimes, rock physics knowledge is used to guide the selection process. Here, we follow the method proposed by Chen and Niu (2022) and use the trend of velocity gradient to determine these representative values. According to the method, each CZ layer is characterized by a segment featuring a relatively constant velocity gradient (Chen & Niu, 2022; see red dash lines in Figure 3c). One advantage of this gradient-based method is that the extracted CZ structure is less affected by the inversion

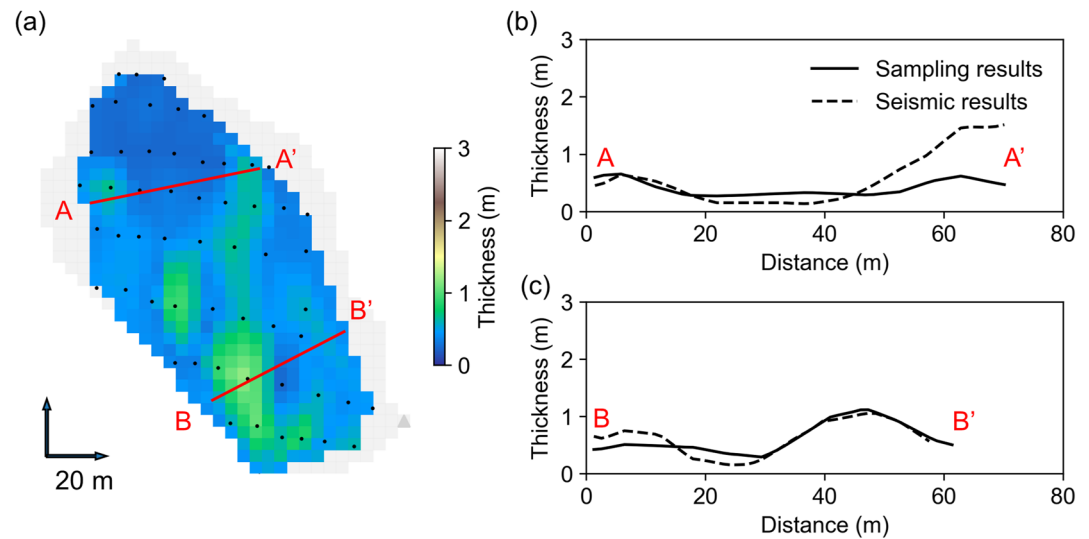


Figure 5. Comparison of seismic velocity-estimated regolith thickness and soil thickness obtained from field soil survey: (a) field soil survey results (Williams et al., 2009), (b) regolith or soil thickness along A-A' transect, and (c) regolith or soil thickness along B-B' transect. In (a), the dots represent the sampling locations, and the contours are plotted with interpolation of the available data points.

process (e.g., the used initial velocity model and applied regularization). This new method is also supported by the distinct velocity-porosity relationships of geological materials observed in different CZ layers (Chen & Niu, 2022). Extracting CZ structures from a typical velocity-elevation profile is demonstrated in Figure 3c, and $v_p = 1.2 \text{ km s}^{-1}$ and 3.5 km s^{-1} are determined as the regolith-fractured bedrock interface and fractured-intact bedrock interface, respectively. Using these values, the locations of the CZ interface in Figure 4a are then determined. In Figures 4c and 4d, the thickness distributions of the regolith and fractured bedrock in the catchment are shown.

In Figure 4c, the regolith thickness ranges from 0 to 2.67 m, and in general, the thickness is larger on ridges than on hillslopes and valley bottoms. The thicker regolith on ridges in Figure 4c is consistent with the prediction from the hillslope model that describes steady-state regolith production as a result of mineral dissolution (Lebedeva & Brantley, 2013). The regolith thickness determined from velocity shows a similar spatial pattern with field soil survey results (Figure 5a; Williams et al., 2009). To better compare the field-measured soil thickness to geophysics-determined regolith thickness (including both soil and saprolite), we plotted both thicknesses along two transects in the catchment (red lines in Figure 5a) in Figures 5b and 5c. As shown in the figures, the general trend of soil thickness along the hillslopes is similar to the velocity-determined regolith thickness. In particular, the regolith thickness on the west ridge on A-A' transect and the east ridge on B-B' transect agrees well with the field sampling results. Some large discrepancies ($>0.5 \text{ m}$) are found on the east ridge on A-A' (e.g., at a distance $>45 \text{ m}$ in Figure 5b), where the velocity-determined regolith thickness is overall higher than the field sampling results. Several factors could contribute to these discrepancies. First, in the soil survey (Williams et al., 2009), the depth was measured by pounding a steel rod through the soil profile to refusal; however, this refusal depth (i.e., soil depth) may be less than the depth with a sharp velocity change that defines the regolith depth in our method (Figure 3c). Second, the previous field soil survey mostly focused on the soil depth on hillslopes (Williams et al., 2009), and only a few data points were available at the valley bottom (Figure 5a). The interpolated values shown in Figure 5b may have high uncertainties. In the field, we observed that the fractured rock is sometimes exposed near the valley bottom; this observation is consistent with the small regolith thickness near the valley bottom as determined from the velocity model (Figures 5b and 5c).

The thickness of fractured bedrock ranges from 0.2 to 45 m (Figure 4d), and its spatial distribution resembles the regolith. We do not have any field data to verify the velocity-estimated fractured bedrock thickness. Borehole results of a different granitic site with a similar climate (Flinchum et al., 2018) show that the fractured granite has a maximum thickness of $\sim 50 \text{ m}$, which is similar to our site. Moreover, the lower boundary geometry of the fractured bedrock seems to be consistent with the predictions of the stress-control theory of CZ development (e.g., Moon et al., 2017; St. Clair et al., 2015) as discussed in Section 3.1.

Table 1

Summary of the Subsurface Models Used in the Study, Including the Geometry of Subsurface Structures, Calibrated Hydrologic Model Parameters, and the Lower Boundary Flow Condition

Model cases	Regolith				Fractured bedrock				Intact bedrock			Lower boundary	
	H_t	K_v	ϕ	K_v/K_h	H_t	K_v	ϕ	K_v/K_h	H_t	K_v or K_h^a	ϕ	Flow condition	C
1	U ^b (2 m)	0.40	0.27	1.1	–	–	–	–	–	–	–	No flow	–
2	V ^c	0.10	0.50	51.5	–	–	–	–	–	–	–	No flow	–
3 ^d	V	0.62	0.42	8.7	30	0.0097	0.18	1	–	–	–	Head-dependent flow	0.0005
4	V	0.32	0.35	12.1	V	0.007	0.27	1.3	30	0.0004	0.09	Head-dependent flow	0.001

Note. H_t is the thickness [m], K_v is the vertical saturated hydraulic conductivity [m d^{-1}], ϕ is porosity [$\text{m}^3 \text{m}^{-3}$], K_v/K_h is the ratio of K_v over horizontal saturated hydraulic conductivity K_h , and C is the conductance [s^{-1}] appearing in the equation calculating deep infiltration (Equation 4).

^aIn intact bedrock, K_v is equal to K_h . ^bU indicates a uniform thickness. ^cV indicates a spatially varied thickness distribution determined from a velocity model. ^dIn Case 3, the nature of the bedrock was not predefined in the modeling. The calibrated parameters were listed in the column of fractured bedrock because they are representative to fractured bedrock.

4. Hydrologic Modeling

In this study, the physically-based hydrologic modeling code MODFLOW 6 (Bakker et al., 2016; Hughes et al., 2017; Langevin et al., 2017) is used to simulate the water partitioning in the catchment. Although MODFLOW was initially designed to simulate groundwater flow and storage, the code has been updated to include various packages that consider surface-groundwater interaction (Daoud et al., 2022) and water dynamics in the unsaturated zone (Daoud et al., 2022). In MODFLOW 6, the unsaturated-zone flow (UZF) package is used to simulate the vadose zone processes. In the UZF package, vertical unsaturated flow is simulated by solving the Richards' equation, which can be coupled at the ground surface with the kinematic wave equation for channel and overland-flow simulation (Charbeneau, 1984). The Brooks-Corey models (R. H. Brooks & Corey, 1966) are used to describe the water retention curve and the unsaturated hydraulic conductivity function.

In addition, the streamflow routing (SFR) package was used to simulate the streams in the MODFLOW model. Relevant model parameters include reach length, width, slope, Manning coefficient, bed level, bed thickness, and bed hydraulic conductivity. These parameters are either determined from a topography map or empirically estimated. The water mover package (MVR) was also used to track the groundwater discharge and the rejected infiltration contributing to the nearest downhill stream reach. This enables an easy estimation of the relative contribution of groundwater and surface runoff to the streamflow. To simulate deep drainage, the general-head boundary (GHB) package was used to account for the head-dependent water flux leaving the catchment through the lower boundary of the model. The implementation of SFR and MVR packages in the MODFLOW model of this study is explained in Text S1 of Supporting Information S1, and the technical details of these packages can be found in the manual of MODFLOW 6 (Hughes et al., 2017). The model files related to the hydrologic modeling are provided in Chen et al. (2023).

4.1. Model Setup and Boundary Conditions

In MODFLOW models, the subsurface needs to be parameterized as different hydrostratigraphic units. The hydrologic properties such as porosity, hydraulic conductivity, and water retention properties are usually kept constant within each hydrostratigraphic unit, and their values can be determined through calibration procedures using field measurements, for example, streamflow. In this study, the regolith, weathered bedrock, and intact bedrock are treated as three hydrostratigraphic units, and the boundaries between two adjacent units (i.e., regolith-fractured bedrock interface and fractured-intact bedrock interface) are determined by their representative velocity contour lines (i.e., $v_p = 1.2 \text{ km s}^{-1}$ and 3.5 km s^{-1} as discussed in Section 3.3). By doing this, the heterogeneous depth distribution of the regolith bottom and weathered bedrock bottom are incorporated into hydrologic modeling. The model with realistic geometries of the subsurface CZ structures is referred to as Case 4 in this study (Table 1).

Many previous hydrologic models do not consider the heterogeneous depth distribution of regolith and weathered bedrock. To study the potential influence, we also designed three models that have simplified subsurface CZ structures. As shown in Table 1, Case 1 only has a regolith layer with a constant thickness sitting on impermeable

rock; this uniform regolith model has been commonly used in hydrologic modeling (e.g., Fullhart et al., 2019). Case 2 also has a regolith layer with an impermeable lower boundary, but the regolith thickness is realistic and determined from the seismic velocity model (i.e., Figure 4c). A comparison of results from Cases 1 and 2 will reveal the role of regolith geometry in streamflow generation. Case 3 is a two-layer model with a realistic regolith geometry and a bedrock layer; the nature of the bedrock (fractured or intact) is not predefined, and a head-dependent flow condition is applied to the bottom of the bedrock. By comparing Case 3 and Case 4, we can explore whether dividing the bedrock into two layers (fractured and intact bedrock) could improve the hydrologic modeling. In Figure S2 of Supporting Information S1, the geometry of subsurface CZ structures of the four models is demonstrated for a typical transect.

The amount of precipitation that falls as snow is considerable at our site. For snows, there is a lag between precipitation and snowmelt (or surface water input, SWI). To calculate SWI, the SNOW-17 model (Anderson, 2006) is used to simulate the observed SWE. This model uses air temperature as an index to determine the energy exchange at the snow-air interface such that the precipitation can be partitioned into snow accumulation as SWE and melt as SWI. The model was calibrated for our site using field-measured snow depth and snow density at a nearby site (Franz et al., 2008). The calibrated model parameters and their uncertainties are provided in Table S2 of Supporting Information S1. The simulated SWE is shown in Figure 2d as solid lines, which are generally in good agreement with the field-measured SWE (cross in Figure 2d). Note that the measured SWE is calculated as the product of the measured snow depth and the measured snow density (Boe, 2013).

In MODFLOW, the calculated SWI from Snow-17 and the potential ET (ET_p) estimated from the Penman-Monteith equation were imposed on the top boundary of the model. No flow was allowed at the vertical boundaries of the catchment. A head-dependent water flux boundary was assigned to the bottom of the bedrock in Cases 3 and 4 to simulate the deep drainage. In the simulation, the flux related to deep drainage at the lower boundary Q_d [$m\ s^{-1}$] can be expressed as (Broda et al., 2011),

$$Q_d = C(h - h_1), \quad (4)$$

where h is the total head at the boundary, h_1 is a head threshold below which groundwater will not drain, and C [s^{-1}] is the conductance or specific leakage at the boundary (Delleur, 2006). In Cases 1 and 2, an impermeable boundary is added to the bottom of the regolith, that is, $Q_d = 0$. For all the cases, lateral outflow through regolith, weathered bedrock, and intact bedrock is not allowed, including the outlet of the catchment. Considering the negligible thickness of regolith and weathered bedrock at the outlet (Figures 4c and 4d), the no-lateral flow condition applied at the outlet is consistent with the field conditions.

4.2. Model Calibration

The hydrologic model was calibrated using field observations from September 2011 to August 2013. In all the cases, model initialization was achieved by running a warm-up period with atmospheric forcing from September 2011 to August 2015. The purpose of model initialization is to provide realistic initial conditions for the calibration. The calibration process was carried out using the shuffled complex evolution method (Duan et al., 1994) with the Python package SPOTPY (Houska et al., 2015). The calibrated parameters in this study include vertical saturated hydraulic conductivity K_v , porosity ϕ , vertical to horizontal saturated hydraulic conductivity K_h ratio K_v/K_h , and the conductance C at the bottom of the bedrock. In the calibration, the streambed hydraulic conductivity was also adjusted by linking it to the vertical conductivity of the subsurface cells in contact with the stream (Daoud et al., 2022; Niswonger et al., 2006). The three CZ layers are treated as different materials. Other model parameters were not included in the calibration, and their values were either taken from previous studies or assigned based on experiences/lab measurements; their values are shown in Table S3 of Supporting Information S1.

The objective function in calibration only includes the measured stream discharge (surface runoff and subsurface lateral flow). The determined optimal values of the model parameters are listed in Table 1. Note that the calibrated hydraulic conductivity ratio $K_v/K_h > 1$ is consistent with the results from previous studies (Fullhart et al., 2019). The calibrated K_v of the regolith layer is similar for all four cases and is close to the value measured in the lab (Bienvenue, 2021). The porosity ϕ of the regolith, however, varies considerably among the four cases. For example, Case 1 (subsurface has only a soil layer with uniform thickness) has a porosity of 27%, but

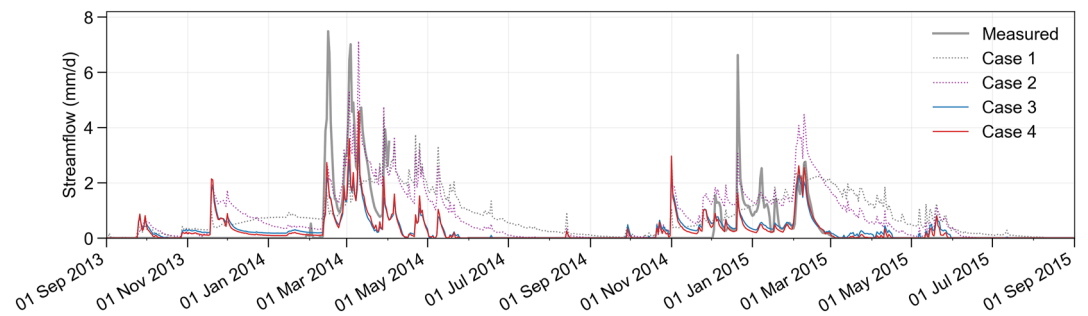


Figure 6. Comparison of predicted streamflow to observed streamflow for water years 2014 and 2015. Four different subsurface models (Cases 1–4) are considered in the simulation and the details of each model can be found in Table 1.

Case 2 (subsurface has only a soil layer with spatially varied thickness) has a much larger porosity (50%). The daily streamflow calculated from the four hydrologic models with their calibrated parameters shows different degrees of agreement with the observations (Figure S3 in Supporting Information S1). In general, the streamflow in Cases 1 and 2 are overestimated; this is consistent with some previous simulations that did not include deep drainage (e.g., Fullhart et al., 2019; Kormos et al., 2015). In contrast, Cases 3 and 4, which include the leakage at the bedrock bottom, are more consistent with the observed discharge (Figure S1 in Supporting Information S1). We also calculate the RMSD between simulated and measured daily discharge. The two models considering the bedrock layer and deep infiltration (i.e., Cases 3 and 4) give a much better fit to the streamflow with RMSDs of 0.52 mm/d and 0.52 mm/d. In contrast, models that assume no-flow conditions for the bottom of regolith (i.e., Cases 1 and 2) cannot accurately reproduce the streamflow. Their associated RMSDs are 0.85 mm/d and 0.68 mm/d, respectively.

4.3. Comparison of Predictions to Observations

We evaluate the predictive capability of the four models by comparing their simulated streamflow to observations in water years 2014 and 2015 (Figure 6). Similar to calibrations, the predictions from Cases 1 and 2 overestimate the discharge, probably due to the lack of deep drainage and/or water storage in the bedrock. The related RMSDs are 0.91 mm/d for Case 1 and 0.80 mm/d for Case 2. The predicted discharge from Cases 3 and 4 shows a similar trend and magnitude with the observations and the associated RMSDs are 0.72 mm/d and 0.69 mm/d, respectively. These results lend further support to the conclusion that hydraulic modeling with realistic subsurface structures may well reproduce the streamflow.

5. Hydrological Partitioning Results

In this section, we discuss the hydrologic modeling results of Case 4 with a particular focus on hydrological partitioning in the CZ. The uncertainties related to the water partitioning analysis are also presented.

5.1. Partitioning of Precipitation in the Catchment

In a headwater catchment, the precipitation P (including both rainfall and snowfall) during a time period is partitioned into several components, expressed as

$$P - (ET_a + Q + I) = \Delta S_a + \Delta S_b, \quad (5)$$

where Q is the stream discharge that is contributed from both surface runoff and subsurface lateral flow, I is the deep infiltration (or deep drainage) through bedrock, and ΔS_a and ΔS_b are the change in water storage above and below ground during the time period, respectively. No pond exists in the catchment, and the only significant above-ground water storage is SWE.

Weekly variations of each component in Equation 5 are plotted in Figure 7 for the catchment during the water year 2014. During this period, most precipitation occurred from Jan 2014 to May 2014 as snow. There was limited rainfall from June 2014 until September 2014. Streamflow was minimal from late June to October and

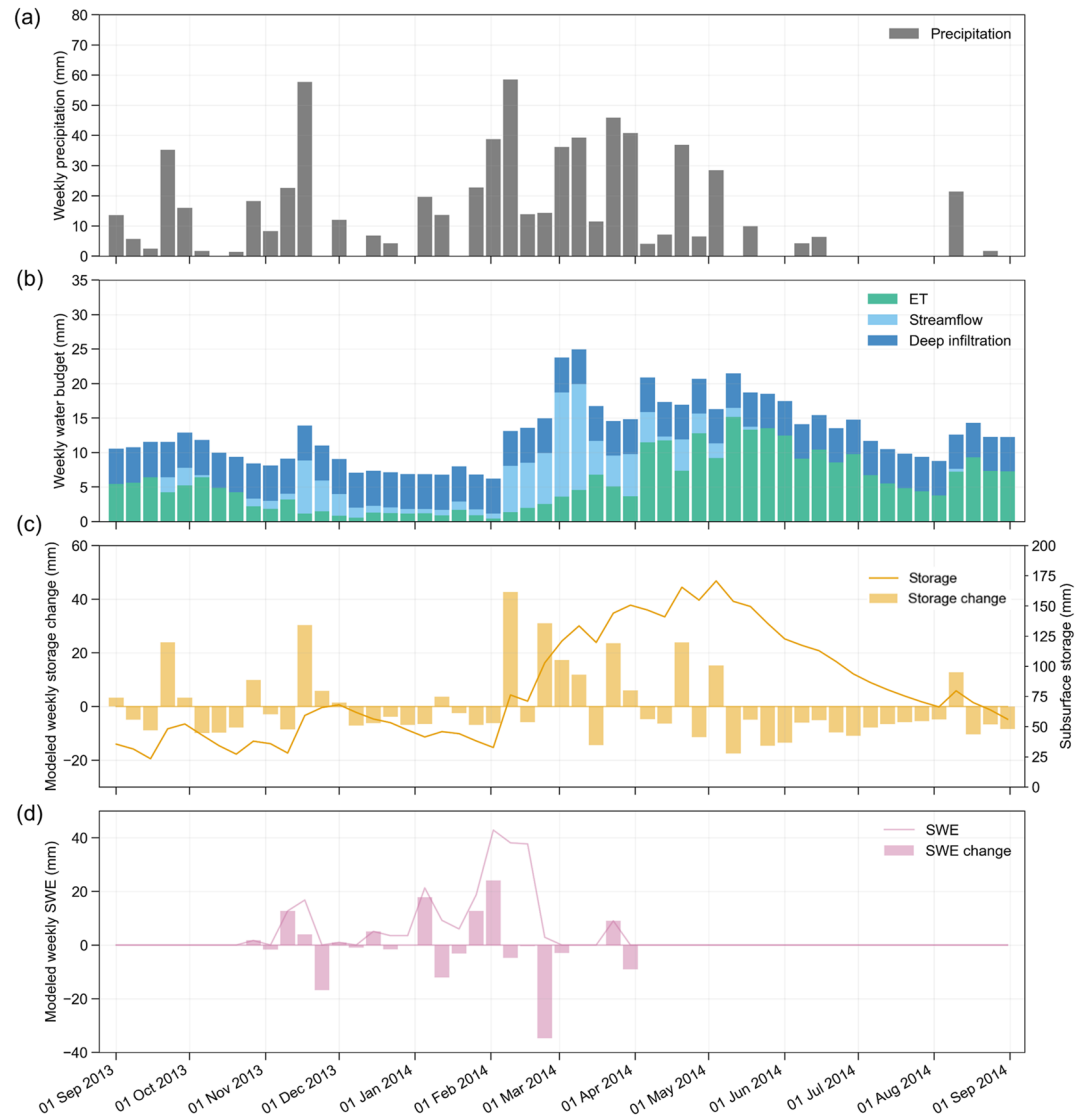


Figure 7. The simulated hydrological partitioning results of the catchment for the water year 2014: (a) weekly precipitation, (b) weekly evapotranspiration (ET), streamflow discharge, and deep infiltration, (c) weekly subsurface storage and its change, and (d) weekly snow water equivalence (SWE) and its change. The simulation results are from the hydrologic model Case 4. In (c), the subsurface storage is the dynamic storage, which is the total subsurface water storage subtracted by the minimum storage during the water year.

was significant during the late spring and early summer. From February to April, the weekly discharge accounts for nearly 50% of the weekly precipitation (Figures 7a and 7b). For example, in the first week of March 2014, the streamflow is 15.1 mm, about 42% of the precipitation (36.2 mm). The time of peak streamflow (early March, Figure 7b) is consistent with the time when the air temperature increases sharply (Figure 2b), implying that the snowmelt runoff may be the primary source of the peak flows (McNamara et al., 2018). Also the peak flow (second week in March) and the peak precipitation (second week in February) are not synchronized (Figure 7). The lag between peak flow and precipitation (mainly snow) is typical for a snow-dominated catchment or a catchment receiving a mix of rain and snow (Kampf & Lefsky, 2016). In total, the calculated annual streamflow accounts for 16.7% of annual precipitation, which is similar to the value determined from field observations (Aishlin & McNamara, 2011).

Plant water use (actual ET) shows a clear seasonal variation (Figure 7b). During the winter time (November to February), ET is energy limited and only accounts for a small portion (<8%) of the precipitation. In the spring (from March to May), ET increases significantly due to temperature increase and adequate subsurface water

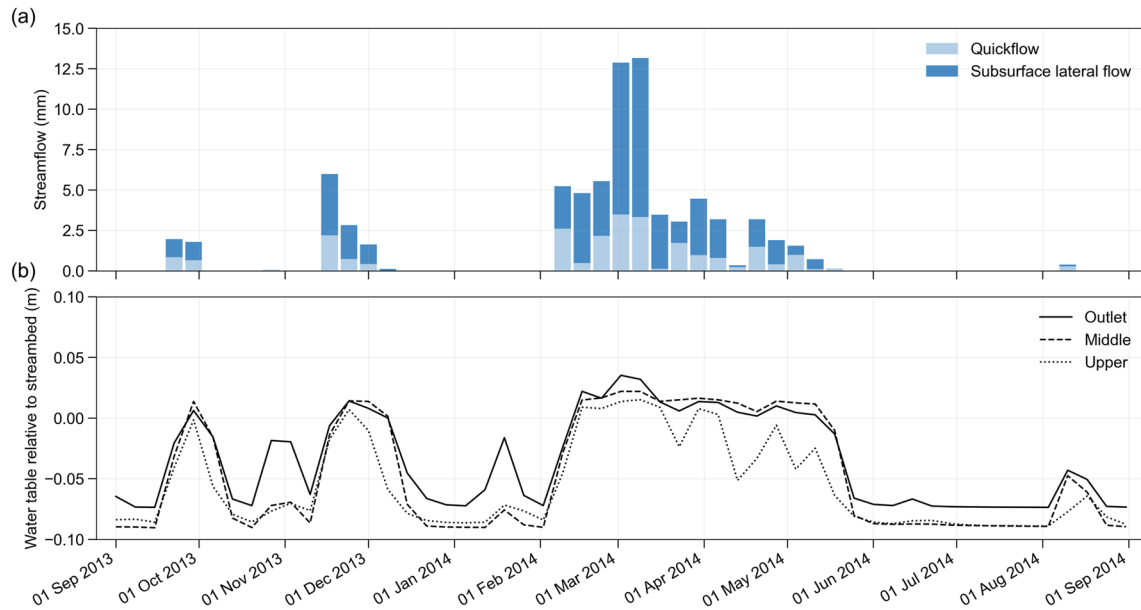


Figure 8. Individual contributions to streamflow for the water year 2014: (a) weekly streamflow and its quickflow and subsurface lateral flow components, (b) groundwater level relative to the streambed at three locations in the catchment (red crosses in Figure 4b): catchment outlet (1,596 m), middle elevation (1,606 m), and upper elevation (1,618 m). The simulation results are from the hydrologic model Case 4.

supplies (solid line in Figure 7c). During this period, ET is about half of the precipitation. In early May, both ET and subsurface water storage reached their peaks and more than 75% the precipitation was consumed by ET. While the driving force (e.g., air temperature, vapor pressure, and solar radiation) for ET is the largest in July, the actual ET decreases significantly during this period, resembling the decreasing trend of the subsurface water storage (solid line in Figure 7c). This highlights the limiting effect of water availability in the subsurface. Using simulation results, annual ET is estimated to be about 43% of annual precipitation, which is consistent with the value reported in other studies (Aishlin & McNamara, 2011).

The changes in the subsurface storage (Figure 7c) reveal a complex interaction between subsurface water storage, precipitation, and ET. Subsurface water is recharged episodically from some large precipitation events during the water year. For example, the largest weekly recharge was the second week in February, during which the catchment received the largest weekly precipitation (~60 mm). At most times of the year, the subsurface water storage decreases over time due to a combined effect of ET, streamflow, and deep infiltration. Deep infiltration is relatively stable throughout the year (Figure 7b) as it is primarily influenced by the groundwater level (Equation 4), which does not change significantly within a water year (Figure 8b). The calculated annual deep bedrock infiltration is approximately 39% of the annual precipitation, which is consistent with a previous study with chloride mass balance estimation and hydrologic modeling (Aishlin & McNamara, 2011; Kormos et al., 2015).

In addition to subsurface water storage, the above-ground water storage (i.e., SWE) and its weekly changes are also plotted (Figure 7d). The largest decrease in SWE (~30 mm) was during the fourth week of February, and it contributed directly to the increase in streamflow observed in the first week of March. The second largest snowmelt event (i.e., ~20 mm during the fourth week of November) did not contribute directly to streamflow generation since no increase in discharge was observed (Figure 7b). Instead, the snowmelt water entered the soil layer, increasing the subsurface water storage by ~5 mm (Figure 7c). Comparing Figure 7d to Figure 7b clearly shows that the peak flow (second week of April) lags ~3–4 weeks behind the maximum snow accumulation time (first week or March).

In summary, the geophysics-informed hydrologic modeling gives similar results as field observations or results from other approaches regarding seasonal variations of ET, streamflow, and deep infiltration. Although there are no measured subsurface water storage data to permit a direct comparison, the calculated variations are consistent with the observed changes in ET, streamflow, and SWE if considering the water budget. Due to the explicit water partitioning results, geophysics-informed hydrologic modeling developed in this study has the potential to provide valuable information for a better understanding of water partitioning in the CZ.

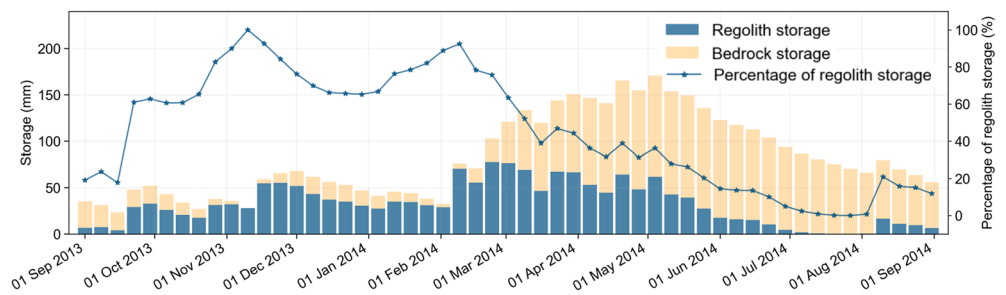


Figure 9. Weekly soil water storage and rock water storage for the water year 2014. The simulation results are from hydrologic model Case 4. The rock water storage is the dynamic storage calculated as total rock water storage subtracted by the minimum storage during the water year.

5.2. Individual Contributions to Streamflow

In the western United States, understanding the sources of streamflow is critical for effectively managing water resources (Kisi et al., 2012). Streamflow contribution includes subsurface lateral flow and quickflow (short-term surface runoff). The traditional way to distinguish them from hydrographs is to conduct a flow separation analysis (e.g., Eckhardt, 2008). In MODFLOW, quickflow can be easily separated from streamflow by quantifying the so-called rejected infiltration, including infiltration excess and saturation excess during or after rainfall or snowmelt (i.e., surface runoff). Subsurface lateral flow is the water discharging to the stream that flows through the regolith or bedrock layer. In this study, the subsurface lateral flow is calculated as streamflow subtracting the surface runoff. The calculated quickflow and subsurface lateral flow in the water year 2014 are shown in Figure 8a.

As shown in Figure 8, quickflow varies significantly during the year and is usually associated with rainfall or snowmelt. For example, the large quickflow in the first two weeks in April (~4 mm) is the result of the largest snowmelt (~35 mm) occurred in late March (Figure 8a). Despite the significant contribution from quickflow, subsurface lateral flow still dominates the streamflow. In particular, during the snowmelt reason (e.g., March), the weekly subsurface lateral flow reaches a peak value, ~10 mm, which is about two times of the quickflow. For rainfall season (e.g., May), the quickflow and subsurface lateral flow are comparable, and sometimes the quickflow could surpass the subsurface lateral flow (e.g., first week in May). This contrast in responses between March and May highlights the different roles of snow and rainfall in contributing to streamflow generation. While large rainfalls tend to cause quickflow, most of the snowmelt water reaches the stream through the subsurface (Bales et al., 2011). The results in Figure 8 show that 69% of the streamflow in the catchment originates from subsurface lateral flow, which is consistent with the field observation that shows little or no surface runoff during rainfall or snowmelt. Figure 8b shows the simulated groundwater table (relative to the streambed) at three locations in the catchment (Figure 4b). It is shown that the groundwater level is generally higher than the streambed during the period when subsurface lateral flow is significant (e.g., from February to May). This implies that the subsurface lateral flow to the stream is partly through the saturated zone.

5.3. Soil Moisture and Rock Moisture

Subsurface water storage has two components, soil moisture and rock moisture. While the role of soil moisture in streamflow generation and ecohydrology has been long realized (Ochsner et al., 2013), the importance of rock moisture is only addressed recently (Rempe & Dietrich, 2018). Compared to soil moisture, rock moisture measurement is costly and usually requires borehole-based techniques such as neutron logging or nuclear magnetic resonance logging (e.g., Schmidt & Rempe, 2020). In our hydrologic modeling, the geometry of both soil and rock layers is realistic, and thus it is straightforward to quantify soil and rock moisture dynamics from the simulation results.

The calculated weekly water stored in the soil and rock layers is plotted in Figure 9 for the water year 2014. In this study, we only focus on dynamic rock water storage, which is the water stored in the bedrock above the lowest groundwater level during the year. This dynamic rock storage quantifies the amount of precipitation that actively contributes to the subsurface storage beyond the regolith. To quantify this component, the subsurface

water dynamics need to be accurately simulated throughout the year. Hydrologic models without the complex subsurface CZ structure (e.g., Cases 1, 2, and 3) will give higher uncertainties, and thus, only Case 4 is used for analysis here. The weekly soil water storage in Figure 9 shows a similar trend to the precipitation (Figure 7a). More precipitation is usually associated with larger soil water storage. For example, the high soil water storage from February to April (>50 mm) corresponds to the high precipitation (from ~15 to ~60 mm) during this period; in August, no precipitation happens, and the soil water storage decreases to almost zero. From September to mid-December, rainfall continuously recharges the soil layer and the water storage increases from ~5 mm to about 25 mm. After mid-December, the snowmelt starts to play a critical role. For example, the soil water storage gets the largest increase in mid-December (~30 mm) and early March (~50 mm) due to the two big snowmelt events (Figure 7d). In the snowmelt season (from February to April), soil moisture stays almost constant (slightly decreased), implying field capacity is reached. The depletion of soil water is primarily due to plant water use (ET), which shows a clear increase starting from March. The ET reaches its peak (~12 mm/week) in late May, and the soil water has decreased to the value before the snow season (e.g., mid-November). It is difficult to relate soil moisture to streamflow by analyzing their weekly trend. However, it is interesting to see that the time streamflow ceased is the end of June, at which the soil moisture decreases to a very low value (lower than ~25 mm). At this time, the subsurface lateral flow has become zero (Figure 8). This may imply that in addition to ET, the streamflow also depletes the soil moisture in early summer.

The rock water storage has a distinct weekly variation if compared to soil water storage. As shown in Figure 9, the rock water storage is generally small (less than 30 mm) from September to the end of February. The rock gets recharged mainly in the late snowmelt season after the soil reaches its field capacity (from March to May). This means only when the soil layer reaches its highest storage will water start to recharge the rock layer. The highest rock water storage is about 110 mm in early May, after which the rock water storage decreases over time. This decrease is primarily related to deep drainage (Figure 7b). The rock water may also supply plant water use in later summer (August) as the soil water storage is almost zero, but the ET is still active (Figure 7b). Overall, the weekly rock water storage is not in phase with precipitation or soil moisture. The rock only gets recharged from the regolith after the soil reaches its field capacity. In addition, the subsurface lateral flow and rock water storage do not correlate, implying the subsurface lateral flow may originate from the saturated groundwater. This is supported by the groundwater table data in Figure 8b, where the groundwater table is generally higher than the streambed when the subsurface lateral flow is present (e.g., from February to May).

Our results show that subsurface water storage is complex during a water year. In the first half water year (October to April), most precipitation entering the subsurface is stored as soil water (~80%). In contrast, from the late snowmelt season to the end of the water year, ~80% of the subsurface water storage is rock water. The highest soil water storage during the year is ~99 mm, which is smaller than the estimated water storage capacity (147 mm) in Parham (2015), implying that the soil layer was not fully replenished. The highest rock water storage is about 112 mm during the water year, comparable to the soil storage capacity, highlighting the importance of rock moisture in CZ studies (e.g., Schmidt & Rempe, 2020).

5.4. Uncertainty Analysis

We conducted a Monte Carlo simulation to estimate the uncertainty related to the hydrological partitioning results. We selected 50 realizations of hydrologic modeling from calibration, and their associated RMSDs are the lowest among all the realizations. The model parameter ranges of these 50 realizations are shown in Table S4 of Supporting Information S1. The Monte Carlo sampling was run 500 times, and for each realization, the water partitioning results are analyzed. The statistics of these water budget-related parameters (Figure 8) are then calculated. In this study, we use the standard deviations and/or their percentage of the mean values to quantify the uncertainty.

The Monte Carlo simulation results show that the uncertainty of calculated weekly streamflow, deep infiltration, ET, and subsurface water storage change (Figure 8) are generally low (see Table S5 in Supporting Information S1). The uncertainty of the calculated discharge (i.e., the ratio of standard deviation over the mean value) ranges between 25% and 55% during the year and is generally high during the high flow season. The uncertainty of deep infiltration is mostly constant throughout the year, at ~18%. For ET, the uncertainty is usually small (<9%) except during the dry summer (e.g., August). Subsurface water storage change also has a small uncertainty, ranging between 5% and 30%, similar to simulated streamflow.

We also analyzed the uncertainty associated with different components of streamflow and subsurface water storage. Their weekly values are summarized in Table S6 of Supporting Information S1. For streamflow, the quickflow generally has a higher uncertainty of ~50%. Both subsurface lateral flow and quickflow uncertainty are slightly high in the wet season and low in the dry season. For subsurface water storage, both the calculated soil and rock water storages show a low uncertainty. Their standard deviations are only a few mm in the dry season and ~8 mm in the wet season.

6. Conclusions

This study shows that it is possible to extract 3D heterogeneous subsurface CZ structure from seismic refractions results. The geophysics-obtained thickness distributions of CZ layers agree well with field soil survey results and some popular CZ theories. Incorporating these realistic CZ structures into hydrologic modeling improves the representation of subsurface heterogeneity, thereby helping decrease the discrepancies between observations and simulations during the calibration of hydrologic modeling. Compared to hydrologic modeling using simplified CZ structures, this geophysics-informed hydrologic modeling gives much better performance. The discharge and soil moisture content predicted from this new hydrologic modeling agrees well with the field observations.

This study also demonstrates the usefulness of geophysics-informed hydrologic modeling to study water partitioning in catchment systems by providing various water fluxes/storage properties, such as discharge, ET, deep drainage, and subsurface water storage. The simulated seasonal water fluxes and storages of a small mountainous catchment generally agree with field observations and results from other studies. In addition, geophysics-informed hydrologic modeling can provide valuable water flux/storage data that cannot be directly measured or are too expensive to be implemented in the field. These parameters include individual components of streamflow (quickflow and subsurface lateral flow) and subsurface water storage (soil moisture and rock moisture). In particular, water storage in the rock can be calculated in a straightforward way, providing an effective approach for quantifying this hidden water reservoir and studying its role in the hydrologic cycle. This new approach may also help us understand how the hydrological partitioning in a catchment and in the subsurface will respond to future climate change and projected precipitation regimes such as drought and high temperature.

Data Availability Statement

The hydrometeorological data used in this study can be downloaded from <https://www.boisestate.edu/drycreek/dry-creek-data/> or Chen et al. (2023). The MODFLOW model, seismic refraction travel time data, and velocity model developed in this study are in Chen et al. (2023). Numerical data used in plotting the figures in this paper can be generated from the MODFLOW model and velocity model. All the data and model files may also be downloaded from https://github.com/geohang/Geophysics_informed_models.

References

- Aishlin, P., & McNamara, J. P. (2011). Bedrock infiltration and mountain block recharge accounting using chloride mass balance. *Hydrological Processes*, 25(12), 1934–1948. <https://doi.org/10.1002/hyp.7950>
- Allen, R. G., Pereira, L. S., Raes, D., & Smith, M. (1998). Crop evapotranspiration—Guidelines for computing crop water requirements—FAO Irrigation and drainage paper 56. *FAO, Rome*, 300(9), D05109.
- Anderson, E. A. (2006). *Snow accumulation and ablation model—SNOW-17* (p. 61). US National Weather Service.
- Bakker, M., Post, V., Langevin, C. D., Hughes, J. D., White, J. T., Starn, J. J., & Fienen, M. N. (2016). Scripting MODFLOW model development using Python and FloPy. *Groundwater*, 54(5), 733–739. <https://doi.org/10.1111/gwat.12413>
- Bales, R. C., Hopmans, J. W., O'Geen, A. T., Meadows, M., Hartsough, P. C., Kirchner, P., et al. (2011). Soil moisture response to snowmelt and rainfall in a Sierra Nevada mixed-conifer. *Vadose Zone Journal*, 10(3), 786–799. <https://doi.org/10.2136/vzj2011.0001>
- Bales, R. C., Molotch, N. P., Painter, T. H., Dettinger, M. D., Rice, R., & Dozier, J. (2006). Mountain hydrology of the western United States. *Water Resources Research*, 42(8). <https://doi.org/10.1029/2005wr004387>
- Barnett, T. P., Adam, J. C., & Lettenmaier, D. P. (2005). Potential impacts of a warming climate on water availability in snow-dominated regions. *Nature*, 438(7066), 303–309. <https://doi.org/10.1038/nature04141>
- Bennett, E. H. (1986). Relationship of the trans-Challis fault system in central Idaho to Eocene and Basin and Range extensions. *Geology*, 14(6), 481–484. [https://doi.org/10.1130/0091-7613\(1986\)14<481:rottfs>2.0.co;2](https://doi.org/10.1130/0091-7613(1986)14<481:rottfs>2.0.co;2)
- Bienvenue, T. J. (2021). *Laboratory measurement of electrical and hydraulic properties of regolith over granitic bedrock*. Boise State University Theses and Dissertations.
- Boe, E. T. (2013). *Assessing local snow variability using a network of ultrasonic snow depth sensors*. Boise State University Theses and Dissertations.
- Bourges, M., Mari, J. L., & Jeannée, N. (2012). A practical review of geostatistical processing applied to geophysical data: Methods and applications. *Geophysical Prospecting*, 60(3), 400–412. <https://doi.org/10.1111/j.1365-2478.2011.00992.x>

Acknowledgments

We would like to acknowledge high-performance computing support of the Borah compute cluster (<https://doi.org/10.18122/oit/3/boisestate>) provided by Boise State University's Research Computing Department. H. Chen would like to thank the support from SEG Foundation/Chevron and Gary and Lorene Servos Scholarship. The authors would like to thank the editor, Dr. Kamini Singha, associate editor, Dr. Sander Huisman, and three anonymous reviewers for their constructive review comments, which have significantly improved the quality of a previous version of the manuscript. This study is partially supported by the National Science Foundation under Grant EAR#2054805.

- Broda, S., Paniconi, C., & Larocque, M. (2011). Numerical investigation of leakage in sloping aquifers. *Journal of Hydrology*, 409(1–2), 49–61. <https://doi.org/10.1016/j.jhydrol.2011.07.035>
- Brooks, P. D., Chorover, J., Fan, Y., Godsey, S. E., Maxwell, R. M., McNamara, J. P., & Tague, C. (2015). Hydrological partitioning in the critical zone: Recent advances and opportunities for developing transferable understanding of water cycle dynamics. *Water Resources Research*, 51(9), 6973–6987. <https://doi.org/10.1002/2015wr017039>
- Brooks, R. H., & Corey, A. T. (1966). Properties of porous media affecting fluid flow. *Journal of the Irrigation and Drainage Division*, 92(2), 61–88. <https://doi.org/10.1061/jrcea4.0000425>
- Callahan, R. P., Riebe, C. S., Pasquet, S., Ferrier, K. L., Grana, D., Sklar, L. S., et al. (2020). Subsurface weathering revealed in hillslope-integrated porosity distributions. *Geophysical Research Letters*, 47(15), e2020GL088322. <https://doi.org/10.1029/2020gl088322>
- Camporese, M., Paniconi, C., Putti, M., & McDonnell, J. J. (2019). Fill and spill hillslope runoff representation with a Richards equation-based model. *Water Resources Research*, 55(11), 8445–8462. <https://doi.org/10.1029/2019wr025726>
- Charbeneau, R. J. (1984). Kinematic models for soil moisture and solute transport. *Water Resources Research*, 20(6), 699–706. <https://doi.org/10.1029/wr020i006p00699>
- Chen, H., & Niu, Q. (2022). Improving moisture content estimation from field resistivity measurements with subsurface structure information. *Journal of Hydrology*, 613, 128343. <https://doi.org/10.1016/j.jhydrol.2022.128343>
- Chen, H., Niu, Q., Mendieta, A., Bradford, J., & McNamara, J. (2023). Geophysics-informed hydrologic modeling data (1.0) [Dataset]. Zenodo. <https://doi.org/10.5281/zenodo.7892511>
- Clark, M. P., Fan, Y., Lawrence, D. M., Adam, J. C., Bolster, D., Gochis, D. J., et al. (2015). Improving the representation of hydrologic processes in earth system models. *Water Resources Research*, 51(8), 5929–5956. <https://doi.org/10.1002/2015wr017096>
- Clayton, J. L., Megahan, W. F., & Hampton, D. (1979). *Soil and bedrock properties: Weathering and alteration products and processes in the Idaho batholith, USDA Forest Service research paper INT (USA)*. Department of Agriculture, Forest Service, Intermountain Forest and Range Experiment Station.
- Daoud, M. G., Lubczynski, M. W., Vekerdy, Z., & Francés, A. P. (2022). Application of a novel cascade-routing and infiltration concept with a Voronoi unstructured grid in MODFLOW 6, for an assessment of surface-water/groundwater interactions in a hard-rock catchment (Sardon, Spain). *Hydrogeology Journal*, 30(3), 899–925. <https://doi.org/10.1007/s10040-021-02430-z>
- Delleur, J. W. (Ed.). (2006). *The handbook of groundwater engineering*. CRC Press.
- Diebel, J. (2006). Representing attitude: Euler angles, unit quaternions, and rotation vectors. *Matrix*, 58(15–16), 1–35.
- Dijkstra, E. W. (1959). A note on two problems in connexion with graphs. *Numerische Mathematik*, 1(1), 269–271. <https://doi.org/10.1007/bf01386390>
- Duan, Q., Sorooshian, S., & Gupta, V. K. (1994). Optimal use of the SCE-UA global optimization method for calibrating watershed models. *Journal of Hydrology*, 158(3–4), 265–284. [https://doi.org/10.1016/0022-1694\(94\)90057-4](https://doi.org/10.1016/0022-1694(94)90057-4)
- Eckhardt, K. (2008). A comparison of baseflow indices, which were calculated with seven different baseflow separation methods. *Journal of Hydrology*, 352(1–2), 168–173. <https://doi.org/10.1016/j.jhydrol.2008.01.005>
- Flinchum, B. A., Holbrook, W. S., & Carr, B. J. (2022). What do P-wave velocities tell us about the critical zone? *Frontiers in Water*, 3, 772185. <https://doi.org/10.3389/frwa.2021.772185>
- Flinchum, B. A., Steven Holbrook, W., Rempe, D., Moon, S., Riebe, C. S., Carr, B. J., et al. (2018). Critical zone structure under a granite ridge inferred from drilling and three-dimensional seismic refraction data. *Journal of Geophysical Research: Earth Surface*, 123(6), 1317–1343. <https://doi.org/10.1029/2017jf004280>
- Franz, K. J., Hogue, T. S., & Sorooshian, S. (2008). Operational snow modeling: Addressing the challenges of an energy balance model for National Weather Service forecasts. *Journal of Hydrology*, 360(1–4), 48–66. <https://doi.org/10.1016/j.jhydrol.2008.07.013>
- Fullhart, A. T., Kelleners, T. J., Chandler, D. G., McNamara, J. P., & Seyfried, M. S. (2019). Bulk density optimization to determine subsurface hydraulic properties in Rocky Mountain catchments using the GEOTop model. *Hydrological Processes*, 33(17), 2323–2336. <https://doi.org/10.1002/hyp.13471>
- Gribb, M. M., Forkutsa, I., Hansen, A., Chandler, D. G., & McNamara, J. P. (2009). The effect of various soil hydraulic property estimates on soil moisture simulations. *Vadose Zone Journal*, 8(2), 321–331. <https://doi.org/10.2136/vzj2008.0088>
- Guo, L., Mount, G. J., Hudson, S., Lin, H., & Levia, D. (2020). Pairing geophysical techniques improves understanding of the near-surface critical zone: Visualization of preferential routing of stemflow along coarse roots. *Geoderma*, 357, 113953. <https://doi.org/10.1016/j.geoderma.2019.113953>
- Hahn, W. J., Rempe, D. M., Dralle, D. N., Dawson, T. E., Lovill, S. M., Bryk, A. B., et al. (2019). Lithologically controlled subsurface critical zone thickness and water storage capacity determine regional plant community composition. *Water Resources Research*, 55(4), 3028–3055. <https://doi.org/10.1029/2018wr023760>
- Hayes, J. L., Riebe, C. S., Holbrook, W. S., Flinchum, B. A., & Hartsough, P. C. (2019). Porosity production in weathered rock: Where volumetric strain dominates over chemical mass loss. *Science Advances*, 5(9), eaao0834. <https://doi.org/10.1126/sciadv.aao0834>
- Houska, T., Kraft, P., Chamorro-Chavez, A., & Breuer, L. (2015). SPOTting model parameters using a ready-made python package. *PLoS One*, 10(12), e0145180. <https://doi.org/10.1371/journal.pone.0145180>
- Hughes, J. D., Langevin, C. D., & Banta, E. R. (2017). Documentation for the MODFLOW 6 framework: U.S. Geological Survey Techniques and Methods (p. 42). <https://doi.org/10.3133/tm6a57>
- Jiang, C., Igel, J., Dlugosch, R., Müller-Petke, M., Günther, T., Helms, J., et al. (2020). Magnetic resonance tomography constrained by ground-penetrating radar for improved hydrogeophysical characterization. *Geophysics*, 85(6), JM13–JM26. <https://doi.org/10.1190/geo2020-0052.1>
- Kampf, S. K., & Lefsky, M. A. (2016). Transition of dominant peak flow source from snowmelt to rainfall along the Colorado Front Range: Historical patterns, trends, and lessons from the 2013 Colorado Front Range floods. *Water Resources Research*, 52(1), 407–422. <https://doi.org/10.1002/2015wr017784>
- Kelleners, T. J., Chandler, D. G., McNamara, J. P., Gribb, M. M., & Seyfried, M. S. (2009). Modeling the water and energy balance of vegetated areas with snow. *Vadose Zone Journal*, 8(4), 1013–1030. <https://doi.org/10.2136/vzj2008.0183>
- Kelleners, T. J., Chandler, D. G., McNamara, J. P., Gribb, M. M., & Seyfried, M. S. (2010). Modeling runoff generation in a small snow-dominated mountainous catchment. *Vadose Zone Journal*, 9(3), 517–527. <https://doi.org/10.2136/vzj2009.0033>
- Kisi, O., Nia, A. M., Gosheh, M. G., Tajabadi, M. R. J., & Ahmadi, A. (2012). Intermittent streamflow forecasting by using several data driven techniques. *Water Resources Management*, 26(2), 457–474. <https://doi.org/10.1007/s11269-011-9926-7>
- Kormos, P. R., Marks, D., Williams, C. J., Marshall, H. P., Aishlin, P., Chandler, D. G., & McNamara, J. P. (2014). Soil, snow, weather, and sub-surface storage data from a mountain catchment in the rain–snow transition zone. *Earth System Science Data*, 6(1), 165–173. <https://doi.org/10.5194/essd-6-165-2014>

- Kormos, P. R., McNamara, J. P., Seyfried, M. S., Marshall, H. P., Marks, D., & Flores, A. N. (2015). Bedrock infiltration estimates from a catchment water storage-based modeling approach in the rain-snow transition zone. *Journal of Hydrology*, *525*, 231–248. <https://doi.org/10.1016/j.jhydrol.2015.03.032>
- Kraft, M., & McNamara, J. P. (2022). Evapotranspiration across the rain–snow transition in a semi-arid watershed. *Hydrological Processes*, *36*(3), e14519. <https://doi.org/10.1002/hyp.14519>
- Langevin, C. D., Hughes, J. D., Banta, E. R., Provost, A. M., Niswonger, R. G., & Panday, S. (2017). MODFLOW 6 modular hydrologic model: U.S. Geological Survey Software. <https://doi.org/10.5066/F76Q1VQV>
- Lebedeva, M. I., & Brantley, S. L. (2013). Exploring geochemical controls on weathering and erosion of convex hillslopes: Beyond the empirical regolith production function. *Earth Surface Processes and Landforms*, *38*(15), 1793–1807. <https://doi.org/10.1002/esp.3424>
- Masaoka, N., Kosugi, K., & Fujimoto, M. (2021). Bedrock groundwater catchment area unveils rainfall-runoff processes in headwater basins. *Water Resources Research*, *57*(9), e2021WR029888. <https://doi.org/10.1029/2021wr029888>
- McNamara, J. P., Benner, S. G., Poulos, M. J., Pierce, J. L., Chandler, D. G., Kormos, P. R., et al. (2018). Form and function relationships revealed by long-term research in a semiarid mountain catchment. *Wiley Interdisciplinary Reviews: Water*, *5*(2), e1267. <https://doi.org/10.1002/wat2.1267>
- McNamara, J. P., Chandler, D., Seyfried, M., & Achet, S. (2005). Soil moisture states, lateral flow, and streamflow generation in a semi-arid, snowmelt-driven catchment. *Hydrological Processes: International Journal*, *19*(20), 4023–4038. <https://doi.org/10.1002/hyp.5869>
- McNamara, J. P., Tetzlaff, D., Bishop, K., Soulsby, C., Seyfried, M., Peters, N. E., et al. (2011). Storage as a metric of catchment comparison. *Hydrological Processes*, *25*(21), 3364–3371. <https://doi.org/10.1002/hyp.8113>
- Mendieta, A. (2017). *Seismic refraction and electrical resistivity tests for fracture induced anisotropy in a mountain watershed* (p. 1351). Boise State University Theses and Dissertations. <https://doi.org/10.18122/B2G71R>
- Miller, C. R., Routh, P. S., Brosten, T. R., & McNamara, J. P. (2008). Application of time-lapse ERT imaging to watershed characterization. *Geophysics*, *73*(3), G7–G17. <https://doi.org/10.1190/1.2907156>
- Moon, S., Perron, J. T., Martel, S. J., Holbrook, W. S., & St. Clair, J. (2017). A model of three-dimensional topographic stresses with implications for bedrock fractures, surface processes, and landscape evolution. *Journal of Geophysical Research: Earth Surface*, *122*(4), 823–846. <https://doi.org/10.1002/2016jg004155>
- Moser, T. J. (1991). Shortest path calculation of seismic rays. *Geophysics*, *56*(1), 59–67. <https://doi.org/10.1190/1.1442958>
- Muhammad, A., Evenson, G. R., Stadnyk, T. A., Boluwade, A., Jha, S. K., & Coulibaly, P. (2019). Impact of model structure on the accuracy of hydrological modeling of a Canadian Prairie watershed. *Journal of Hydrology: Regional Studies*, *21*, 40–56. <https://doi.org/10.1016/j.ejrh.2018.11.005>
- Müller, S., Schüler, L., Zech, A., & Heße, F. (2021). GSTools v1.3: A toolbox for geostatistical modelling in Python. *Geoscientific Model Development Discussions*, 1–33.
- Nielson, T., Bradford, J., Holbrook, W. S., & Seyfried, M. (2021). The effect of aspect and elevation on critical zone architecture in the Reynolds Creek critical zone observatory: A seismic refraction study. *Frontiers in Water*, *3*, 670524. <https://doi.org/10.3389/frwa.2021.670524>
- Nielson, T., Bradford, J., Pierce, J., & Seyfried, M. (2021). Soil structure and soil moisture dynamics inferred from time-lapse electrical resistivity tomography. *Catena*, *207*, 105553. <https://doi.org/10.1016/j.catena.2021.105553>
- Niswonger, R. G., Prudic, D. E., & Regan, R. S. (2006). Documentation of the Unsaturated-Zone Flow (UZFI) package for modeling unsaturated flow between the land surface and the water table with MODFLOW-2005 (No. 6-A19).
- Ochsner, T. E., Cosh, M. H., Cuenca, R. H., Dorigo, W. A., Draper, C. S., Hagimoto, Y., et al. (2013). State of the art in large-scale soil moisture monitoring. *Soil Science Society of America Journal*, *77*(6), 1888–1919. <https://doi.org/10.2136/sssaj2013.03.0093>
- Panicconi, C., & Putti, M. (2015). Physically based modeling in catchment hydrology at 50: Survey and outlook. *Water Resources Research*, *51*(9), 7090–7129. <https://doi.org/10.1002/2015wr017780>
- Parham, W. B. (2015). *Spatial and temporal storage dynamics moderate the ecohydrologic significance of evapotranspiration in semi-arid, mountainous terrain* (p. 946). Boise State University Theses and Dissertations.
- Parsekian, A. D., Singha, K., Minsley, B. J., Holbrook, W. S., & Slater, L. (2015). Multiscale geophysical imaging of the critical zone. *Reviews of Geophysics*, *53*(1), 1–26. <https://doi.org/10.1002/2014rg000465>
- Patton, N. R., Lohse, K. A., Godsey, S. E., Crosby, B. T., & Seyfried, M. S. (2018). Predicting soil thickness on soil mantled hillslopes. *Nature Communications*, *9*(1), 3329. <https://doi.org/10.1038/s41467-018-05743-y>
- Poulos, M. J. (2016). *Feedbacks among climate, soils, vegetation, and erosion drive valley asymmetry development in the mountains of Central Idaho* (p. 1190). Boise State University Theses and Dissertations.
- Rempe, D. M., & Dietrich, W. E. (2018). Direct observations of rock moisture, a hidden component of the hydrologic cycle. *Proceedings of the National Academy of Sciences*, *115*(11), 2664–2669. <https://doi.org/10.1073/pnas.1800141115>
- Reynolds, S. D., Mildren, S. D., Hillis, R. R., Meyer, J. J., & Flottnann, T. (2005). Maximum horizontal stress orientations in the Cooper Basin, Australia: Implications for plate-scale tectonics and local stress sources. *Geophysical Journal International*, *160*(1), 331–343. <https://doi.org/10.1111/j.1365-246x.2004.02461.x>
- Riebe, C. S., Hahm, W. J., & Brantley, S. L. (2017). Controls on deep critical zone architecture: A historical review and four testable hypotheses. *Earth Surface Processes and Landforms*, *42*(1), 128–156. <https://doi.org/10.1002/esp.4052>
- Rücker, C., Günther, T., & Wagner, F. M. (2017). pyGIMLi: An open-source library for modelling and inversion in geophysics. *Computers & Geosciences*, *109*, 106–123. <https://doi.org/10.1016/j.cageo.2017.07.011>
- Schmidt, L., & Rempe, D. (2020). Quantifying dynamic water storage in unsaturated bedrock with borehole nuclear magnetic resonance. *Geophysical Research Letters*, *47*(22), e2020GL089600. <https://doi.org/10.1029/2020gl089600>
- St. Clair, J., Moon, S., Holbrook, W. S., Perron, J. T., Riebe, C. S., Martel, S. J., et al. (2015). Geophysical imaging reveals topographic stress control of bedrock weathering. *Science*, *350*(6260), 534–538. <https://doi.org/10.1126/science.aab2210>
- Wagner, F. M., & Uhlemann, S. (2021). An overview of multimethod imaging approaches in environmental geophysics. *Advances in Geophysics*, *62*, 1–72.
- Webster, R., & Oliver, M. A. (2007). *Geostatistics for environmental scientists*. John Wiley & Sons.
- Williams, C. J., McNamara, J. P., & Chandler, D. G. (2009). Controls on the temporal and spatial variability of soil moisture in a mountainous landscape: The signature of snow and complex terrain. *Hydrology and Earth System Sciences*, *13*(7), 1325–1336. <https://doi.org/10.5194/hess-13-1325-2009>